OPEN

# Structural, Photophysical, and Electronic Properties of CH3NH3PbCl3 Single Crystals

Hao-Ping Hsu[1], Liang-Chen Li[2], Muthaiah Shellaiah[1] & Kien Wen Sun[1,2]

Methylammonium lead chloride ($CH_3NH_3PbCl_3$ or $MAPbCl_3$) single crystals were fabricated using the inverse temperature crystallization method, and their structural, photophysical, and electronic characteristics were studied using temperature dependent optical spectroscopy, X-ray diffraction (XRD), current-voltage, and Hall measurements. The changes in absorption and photoluminescence properties accompanied with structural changes in crystal lattice were studied within a broad temperature range of 300–20 K. XRD investigations reveal that phase changes took placed around 180 K and 175 K. At a temperature below 170 K, two different crystallographic phases were found to co-exist in the photoluminescence spectra. An asymmetric line shape with broad and weak shoulders near the absorption edges was observed in all of the major PL peaks. The weak shoulders are attributed to the missing chloride atoms on the crystal surface. The photoluminescence intensity of the crystals was strongly influenced by the environment, thereby indicating that the carrier recombination is affected by the physical desorption/absorption of gas molecules at the crystal surface. Moreover, vibronic replicas in the photoluminescence spectra at low temperature were observed for the first time. The origins of these replicas are attributed to the coupling between the vibrational/librational motions of the organic cations and the photoexcited electrons. Finally, the Hall and current-voltage measurements confirm that the crystal is an n-type semiconductor with a carrier concentration of ~$2.63 \times 10^{11}\,cm^{-3}$, a mobility of $4.14\,cm^2/V{\bullet}s$, and a conductivity of $1.8 \times 10^{-8}\,\Omega^{-1}cm^{-1}$ under dark and room temperature conditions.

Organic/inorganic hybrid methylammonium lead halide perovskite ($MAPbX_3$) is the most promising energy materials for photovoltaic and optoelectronic applications. Altering the properties of these materials for improvement is obtained by varying the type of metallic or halide ions[1]. $MAPbX_3$ solar cells have progressed in efficiency faster than any other solar cells since their invention[2–5]. Researches in metal-halide perovskites as promising optoelectronic materials for solid-state light emitting applications[6–8] and detectors[9,10] beyond photovoltaics have increased. Metal-halide perovskites are inexpensive solution-processable materials with excellent intrinsic properties that render them appropriate candidates for technologies in the future. However, commercialization of perovskite devices is hindered by rapid material degradation[11,12], hysteresis[13,14], and environmental factors, such as moisture and heat[15]. Even with the outstanding materials properties and device performances of hybrid perovskites, some restrictions must be solved in order to gain intact optoelectronic and sensing applications and commercialization. Understanding the underlying mechanisms behind is necessary to analyze the material and enhance the efficiency, sensitivity, and stability of devices based on these perovskites.

Previous researches focused mostly on polycrystalline perovskite thin films[16–22] for characterizing their material properties. However, the intrinsic electronic or optoelectronic properties of polycrystalline thin films are overshadowed by the micro-, nano- and/or non-crystalline domains. On the other end of the spectrum, perovskite single crystals are an ideal platform for investigating the intrinsic structural and photophysical properties of perovskites because they are free from grains and amorphous domains, thereby improving the efficiency and long-term stability of polycrystalline perovskite optoelectronic and photovoltaic devices.

Compared to perovskite thin films, reports on $MAPbX_3$ single crystals are relatively few. For instance, $MAPbI_3$ and $MAPbBr_3$ single crystals show carrier diffusion lengths over 100 μm and high hole and electron mobilities of 9400 and 2800 $cm^2\text{-}V^{-1}s^{-1}$, respectively[23–25]. α–phase $CH_3NH_3PbBr_3$ bulk crystals studied by spectroscopic

[1]Department of Applied Chemistry, National Chiao Tung University, 1001 University Road, Hsinchu, 30010, Taiwan. [2]Center for Nano Science and Technology, National Chiao Tung University, Hsinchu, 30010, Taiwan. Correspondence and requests for materials should be addressed to K.W.S. (email: kwsun@mail.nctu.edu.tw)
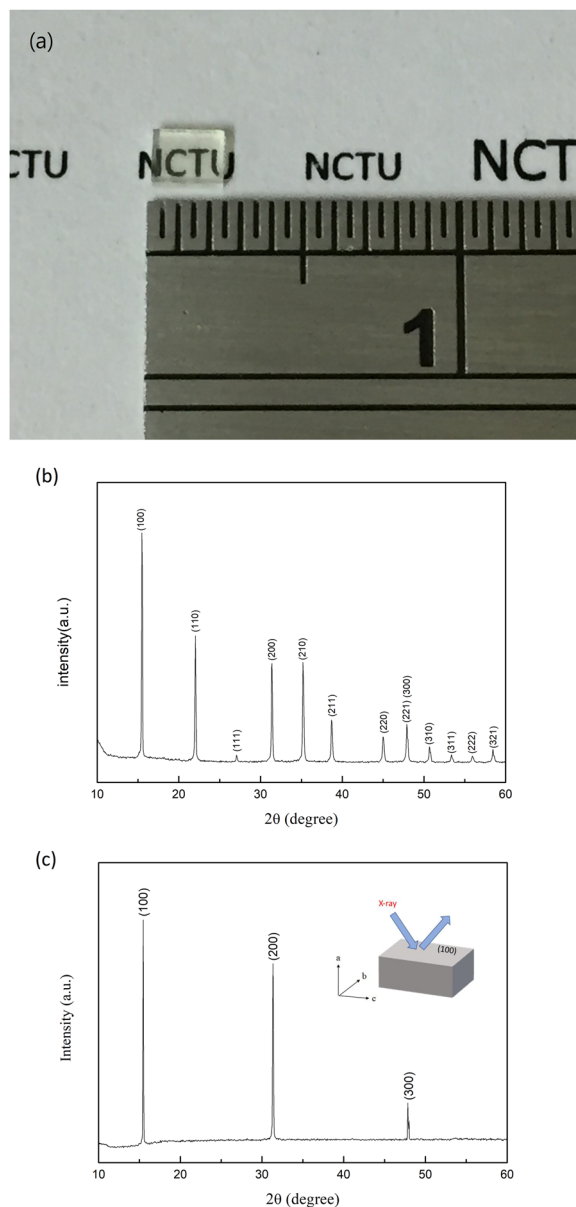
**Figure 1.** (**a**) Optical image of the MAPbCl$_3$ single crystal prepared by the modified ITC method (**b**) powder and (**c**) single crystal XRD patterns of the crystal at room temperature. The inset illustrates the crystal orientation during XRD measurements.

ellipsometry[26] from 0.73–6.45 eV showed a strong optical transition at ~2.3 eV and randomly oriented cations at room temperature. Low trap density and exceptionally long and balanced carrier diffusion lengths were reported in decent-sized MAPbX$_3$ single crystals[27]. The dynamics of photoexcited carriers, such as recombination mechanisms in surface or bulk and carrier diffusion in MAPbBr$_3$ single crystals, was studied using transient optical spectroscopy[28–30]. MAPbBr$_3$ single crystals in the orthorhombic phase were reported to have an exciton binding energy of 15.33 meV and a Bohr radius of ~4.38 nm at a low temperature by Tilchin *et al.*[31]. The optical band gap, carrier recombination, excitation spectra, PL spectral position, and lifetime characteristics of the incipient surface of a MAPbBr$_3$ single crystal are different from that of a pristinely cleaved crystal surface[32]. More recently, structural and photophysical properties of MAPbBr$_3$ single crystals were studied using temperature dependent optical and X-ray diffraction (XRD) techniques[33]. A direct time domain view of large polaron formation in MAPbBr$_3$ single crystals was provided by Miyata *et al.*[34], who revealed that, irrespective of the cation type, the large polaron is formed mainly from the deformation of the PbBr$_3^-$ frameworks.

Despite lead halide perovskite single crystals have been intensively researched, methylammonium lead chloride (MAPbCl$_3$) as an important member in perovskite family, attracts less attention. As a wide bandgap semiconductor, the MAPbCl$_3$ is transparent to visible but responsive to UV radiation; its absorption, which is mainly limited to wavelengths no longer than 400 nm, makes it a suitable candidate for UV applications. These wide bandgap perovskite semiconductors are promising candidates for solution-processed UV light
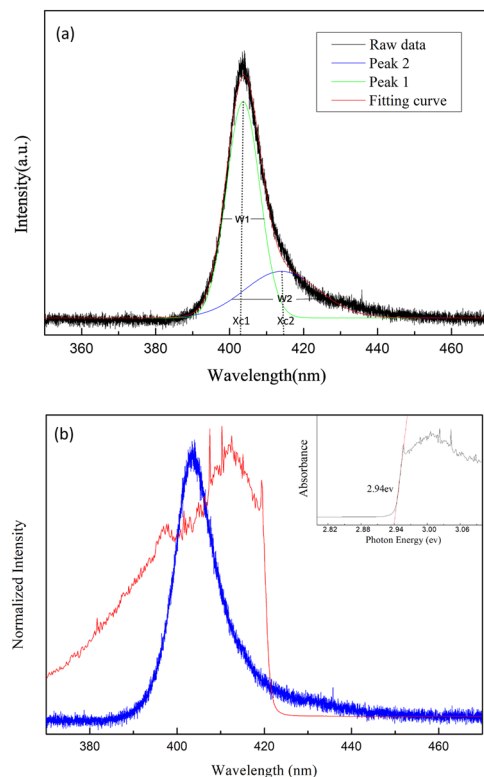
**Figure 2.** (**a**) PL spectrum fitted with peaks 1 and 2 at 300 K. $X_{c1}$, $X_{c2}$, $W_1$, and $W_2$ represent the peak positions and bandwidths at FWHM of peaks 1 and 2, respectively. (**b**) PL and UV-Vis absorption spectra of the MAPbCl$_3$ single crystal excited at 266 nm. The inset shows the Tauc-plot fitting to determine the onset of the absorption.

emitting devices, photodetectors, and transparent electronics. For example, UV photodetectors based on crystalline MAPbCl$_3$ exhibited improved figures of merit by several orders of magnitude[35,36]. Photo response from metal-semiconductor-metal detectors based on MAPbCl$_3$ single crystals showed dependence on the crystal orientations[37]. Future device refinement and advancement of MAPbCl$_3$-based devices could be possible only by further exploring their intrinsic properties, such as a better understanding in crystal structures/energy levels and mechanisms in charge transport and separation. Despite laborious research, opinions regarding these basic properties are inconsistent, and more investigations are required to resolve these dissents.

This study aims to distinguish the intrinsic structural, photophysical, and electronic characteristics between MAPbCl$_3$ single crystals and polycrystalline thin films by focusing on MAPbCl$_3$ single crystals synthesized from solutions, which show less defects and reduced grains. These material properties were investigated using temperature dependent single crystal/powder XRD, continuous wave photoluminescence (PL), absorption/transmittance, Raman spectroscopy, and Hall and current-voltage (I–V) measurements at a wide temperature range.

## Experimental Methods

**General Information.** The crystal structures and phase transitions of the as-grown MAPbCl$_3$ single crystals were investigated by temperature dependent XRD. Single crystal and powder XRD studies were conducted with a Bruker D8 Discover X-ray Diffraction System from 300–20 K. Transmission electron microscopy (TEM) samples and high-resolution TEM (HRTEM) images were obtained using a TESCAN LYRA 3 Dual-Beam Focus Ion Beam Microscope and a JEOL-JEM-2100F, respectively. Temperature dependent absorption/transmittance spectra from room temperature to 20 K were taken using a combination of a HOROBA iHR-550 spectrometer, Xenon lamp, and liquid-nitrogen cooled CCD detector with the samples placed in a thermostat. Temperature dependent continuous wave PL spectra were recorded at 300–20 K with a HOROBA iHR-550 spectrometer, liquid-nitrogen cooled CCD detector, and semiconductor laser operated at 266 nm. A Lab RAM HR instrumental setup using a HOROBA iHR-550 spectrometer and a 532 nm semiconductor laser were employed to conduct Raman investigations at room temperature.

Hall measurements were taken in vacuum with a GMW model 5430 instrument at room temperature with a sample size of ~2.5 mm × 2 mm × 1 mm at a scanned magnetic field up to 0.375 Tesla. The current-voltage (I–V) curves were recorded with an EverBeing model CG-196 two-point and four-point probe station at room temperature with sample placed in dark and/or illuminated with a 405 nm laser.

**Synthesis of MAPbBr3 single crystal.** The inverse temperature crystallization (ITC) method reported in an earlier study[24] was adapted to prepare the MAPbBr$_3$ single crystals from a solution. Lead chloride (PbCl$_2$, 99.999%, Alfa Aesar), methylammonium hydrochloride (CH$_3$NH$_3$Cl, 99%, Alfa Aesar), dimethylformamide
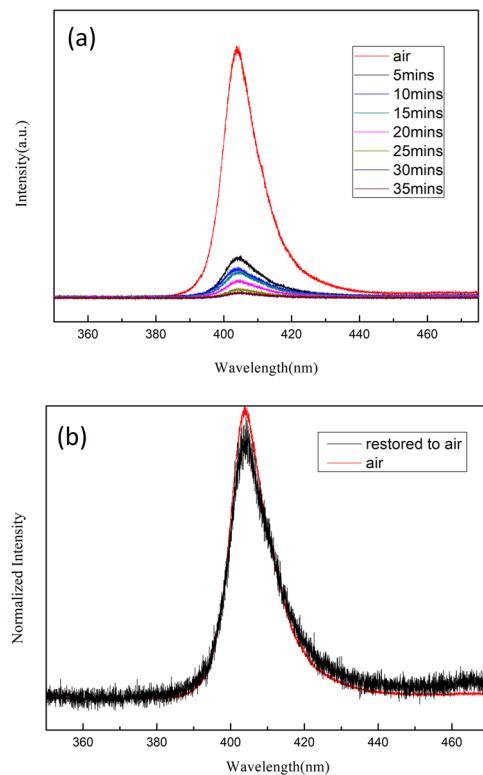
**Figure 3.** (**a**) PL spectra excited at 266 nm at 300 K under ambient and vacuum. The chamber pressure reached ~$10^{-3}$ torr after pumping down for 35 mins. (**b**) Emission intensity was fully recovered after chamber pressure restored to air.

(DMF) ($C_3H_7NO$, 99.5%, Merck KGaA), and dimethyl sulfoxide (DMSO) ($C_2H_6OS$, 99.7%, Sigma-Aldrich) were used as received and without further purification. A total of 0.2228 g of $CH_3NH_3Cl$ were added quickly to 3.3 mL DMSO:DMF (1:1) solution in an ultrasonic bath under a $N_2$ atmosphere at room temperature for 10 min until the $CH_3NH_3Cl$ was totally dissolved. Then, 0.8343 g $PbCl_2$ was added to 3 mL $CH_3NH_3Cl$/DMSO:DMF (1:1) solution and stirred for 20 min until the solution became transparent. The solution was filtered using PVDF filter. The filtrate was placed in a vial and kept in an oil bath undistured at 50 °C for 6 ~8 h till single crystals formed in a size of ~2.5 × 2 mm with a thickness of ~1 mm. Once millimeter-sized single crystals were formed, they were taken out from the vial and dried with a nitrogen gun.

## Results and Discussions

The optical image of a MAPbCl$_3$ single crystal prepared by the modified ITC method with dimensions of ~2.5 × 2 × 1 mm$^3$ is shown in Fig. 1(a). Figure 1(b,c) display the obtained powder and single crystal XRD spectra at room temperature, respectively. The crystal adopted the centrosymmetric $Pm\overline{3}m$ cubic space group at 300 K. The diffraction peak positions (Fig. 1(b)) at 15.71°, 22.22°, 27.24°, 31.58°, 35.38°, 38.86°, 45.18°, 48.09°, 50.85°, 53.52°, 56.07°, and 58.58° were transformed into interplanar distances, which correlated to the (100), (110), (111), (200), (210), (211), (220), (221)(300), (310), (311), (222), and (321) crystal planes, respectively. These results agree with earlier reports[36]. Due to the immediate amorphization or liquidation of the material when exposed to the high energy electron beam, TEM images or selective area electron diffraction (SAED) patterns of the crystal cannot be obtained. The TEM/SEM images of the sample slices prepared with focused ion beam are shown in Fig. S1 in Supporting Information.

The UV-visible PL and absorption spectra of the solution prepared MAPbCl$_3$ single crystal excited with a 266 nm semiconductor laser at 300 K are displayed in Fig. 2. Similar to the previous reports for MAPbBr$_3$ and MAPbI$_3$[25,30,33,38], the PL spectrum was found to be asymmetric in line shape and trailed toward long wavelengths. The line shape of the spectrum can be fitted by two luminescence peaks (Fig. 2(a)). The major emission peak 1 above the absorption edge arose from the interband transition and was at 404 nm (~3.07 eV) with a linewidth of ~11 nm (FWHM). The weaker emission peak 2 with a broad linewidth of 24 nm at 415 nm (~2.98 eV) was resulted from the recombination of photoexcited carriers in defects (Cl vacancies on the crystal surface) below the energy gap. The inset in Fig. 2(b) shows a bandgap of ~2.94 eV using Tauc-plot. Similar to the previous reports in single crystal perovskite[23,27], the mission energy of peak 1 was found to be above the bandgap. Be noted that the absorption lineshape could be affected substantially in a thick sample with strong absorption. Moreover, using Tauc-plot for determining bandgap tends to underestimate the real bandgap value due to the tail absorption[39]. Therefore, to yield an accurate bandgap, the sample thickness needs to be controlled within a few microns.
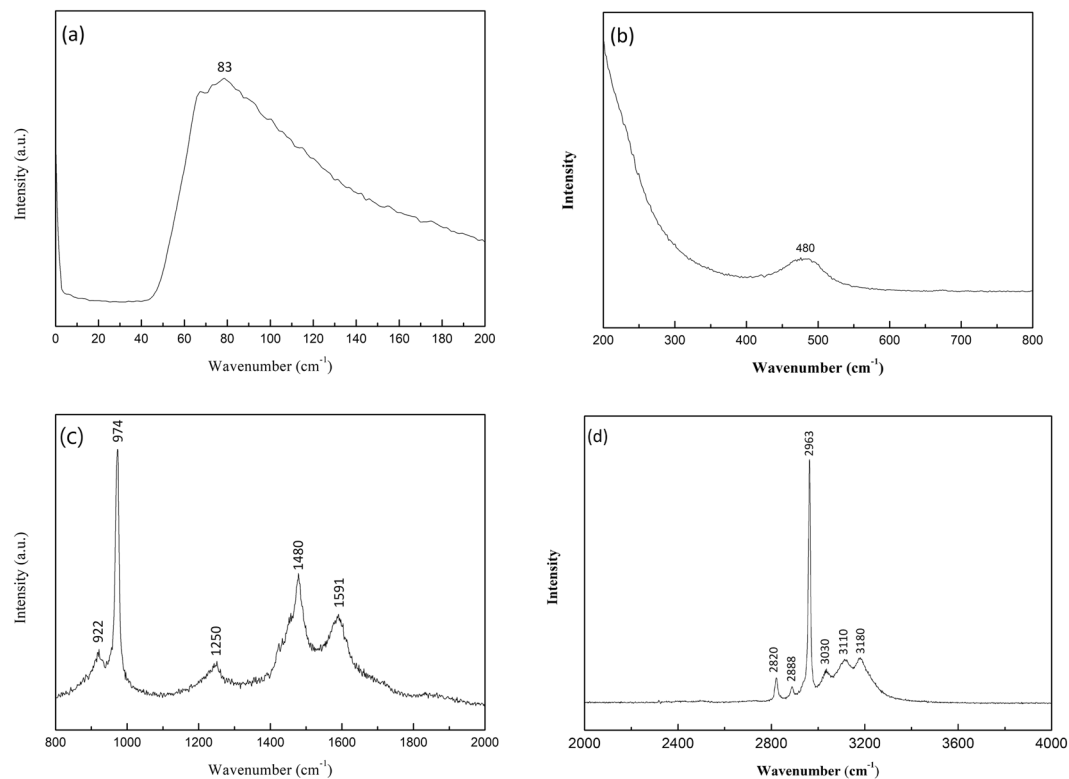
**Figure 4.** Raman spectra of MAPbCl$_3$ single crystals excited at 532 nm at room temperature cover from (**a**) 0–200 cm$^{-1}$ (**b**) 200–400 cm$^{-1}$ (**c**) 800–2000 cm$^{-1}$ and (**c**) 2000–4000 cm$^{-1}$.

| MAPbCl$_3$ (cm$^{-1}$) | Peak assignment |
|---|---|
| 480 | CH$_3$NH$_3^+$ torsion |
| 922 | CH$_3$NH$_3^+$ rocking |
| 974 | C–N stretching |
| 1250 | CH$_3$-NH$_3^+$ rocking |
| 1480 | asym. NH$_3^+$ bending |
| 1591 | NH$_3^+$ twisting |
| 2820 | N$^+$–H stretching |
| 2888 | Asym. CH$_3$ stretching |
| 2963 | Sym. CH$_3$ stretching |
| 3030 | NH$_3^+$ Sym. stretching |
| 3110 | |
| 3180 | |

**Table 1.** The measured Raman peaks of the MAPbCl$_3$ single crystal and assignment of corresponding vibration modes.

We then studied the PL intensity behavior of peak 1 to find out the environmental effect on the photogenerated carriers in the MAPbCl$_3$ single crystals. The recorded PL spectra excited by a 266 nm semiconductor laser at 300 K in ambient and vacuum (~10$^{-3}$ torr after pumping down for 35 mins) are shown in Fig. 3(a). The PL intensity began to drop when the chamber pressure was lowered toward 10$^{-3}$ torr. However, the PL intensity was fully recovered when the chamber pressure was restored as shown in Fig. 3(b). This result suggested that the carrier recombination is possibly affected by the physical desorption/absorption of gas molecules on the crystal surface. Therefore, the surface of the MAPbCl$_3$ single crystal is sensitive to the environment. Recent investigations also indicated that the interplay between hybrid perovskites and environments considerably affect the material's morphological properties or photostability and its optoelectronic properties[23,29,30,33,40,41].

To prevent the effect of fluorescence background, a 532 nm semiconductor laser was used in the Raman measurements to study the interaction between the MA$^+$ cation and the PbCl$_6^-$ in the octahedral framework. Figure 4(a–d) shows the Raman spectra recorded with a high signal-to-noise ratio and a wavenumber range of 0–4000 cm$^{-1}$ from a MAPbCl$_3$ single crystal. In Fig. 4(a), the Raman band at a frequency of 83 cm$^{-1}$ can be
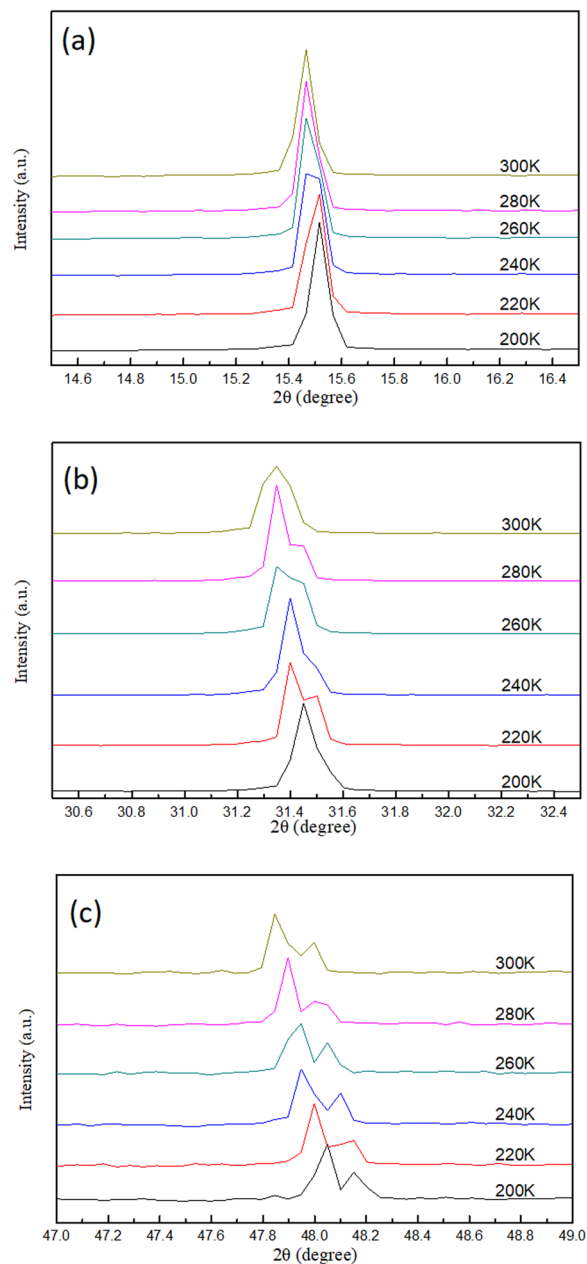
**Figure 5.** Diffraction spectrum of (**a**) (100) (**b**) (200) and (**c**) (300) peak from single crystal XRD measurements of MAPbCl$_3$ single crystal at 300–200 K.

attributed to the artifact from the filter cutoff[42,43]. However, the Raman peak at 480 cm$^{-1}$ shown in Fig. 4(b) was corresponded to the limited rotation of the cation in MAPbCl$_3$. The middle- and higher-energy peaks displayed in Fig. 4(c,d) were all associated to the various types of the MA$^+$ movements. For instance, the distinct and sharp peaks at 922 cm$^{-1}$ and 974 cm$^{-1}$ were originated from the CH$_3$NH$_3^+$ rocking and C-N stretching, correspondingly. The intense peak at 2963 cm$^{-1}$ was associated to the symmetric stretching of CH$_3$. The assignments of Raman peaks from MAPbCl$_3$ single crystals, which are in good agreement with earlier reports[44–46], are summarized in Table 1. For the lead halide perovskites with atoms of electronegativity strengthens from weakest (I) to strongest (Cl), although the magnitude of the Raman peaks was nearly unchanged, nontheless, either blueshift or redshift in energy could be detected for Raman modes[33,44–46]. These observations indicated that substituting halide atoms with high electronegativity strengthens significantly modifies the microenvironment of the PBX$_3^-$ framework.

The temperature dependent structural properties of the MAPbCl$_3$ single crystal were analyzed based on temperature dependent absorption/PL spectra and XRD measurements from 300 K to 20 K. Fig. S2(a,b) in Supporting Information display the transitions of the powder and single crystal XRD patterns of the crystal recorded from 300–20 K, respectively. The crystal underwent two structural changes, which associated to the first phase transition from cubic to tetragonal (at temperatures between 200–180 K) followed by a second phase transistion from
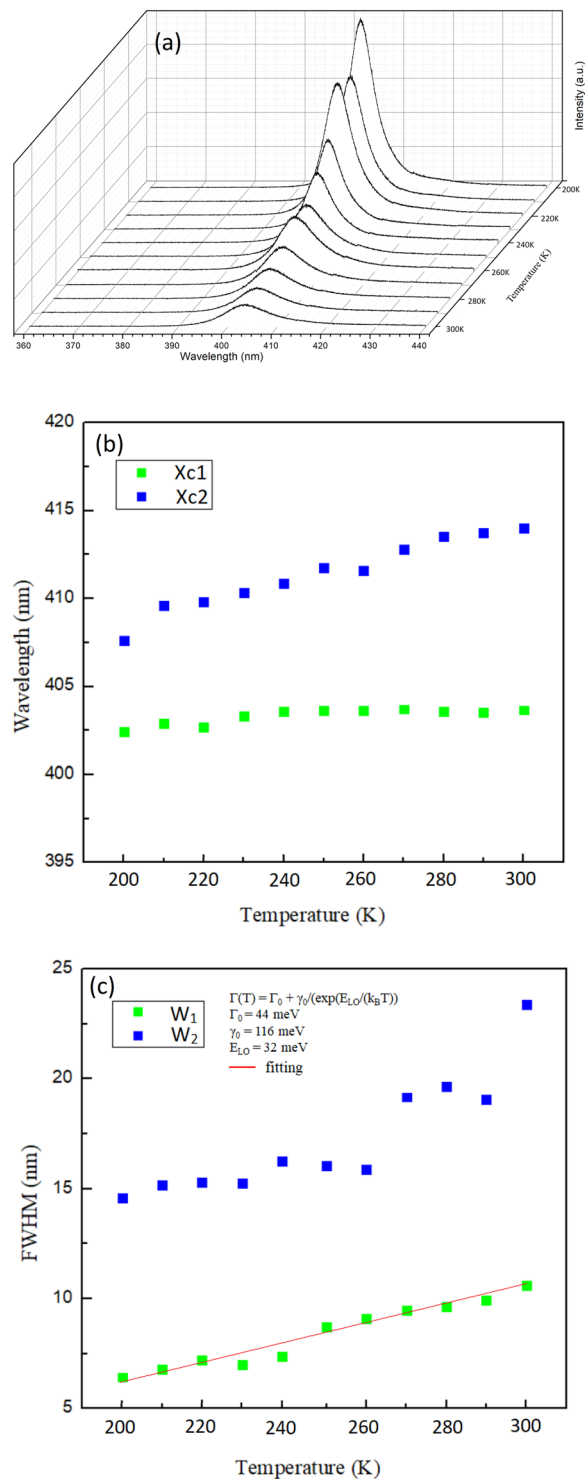
**Figure 6.** (**a**) Temperature dependent PL spectra of MAPbCl$_3$ single crystal excited at 266 nm at 300–200 K. The PL spectra were fitted with peaks 1 and 2 as in Fig. 2(a). X$_{c1}$, X$_{c2}$, W$_1$, and W$_2$ represent the peak positions and bandwidths at FWHM of peaks 1 and 2. Temperature dependent (**b**) peak positions (X$_{c1}$, X$_{c2}$) and (**c**) bandwidths (W$_1$, W$_2$) of peaks 1 and 2. The red-colored fitting curve in (**c**) is obtained by using the formula displayed in the inset.

tetragonal to orthorhombic (at temperatures between 175–170 K). These phase changes were occurred simultaneously with shifts in energy and changes in line shape in the absorption and PL spectra (Fig. S3 in Supporting Information). In the following sections, we categorized and discussed in detail the temperature dependent structural transitions in three temperature ranges as follows: 300 K to 200 K, 200 K to 170 K, and 160 K to 20 K.
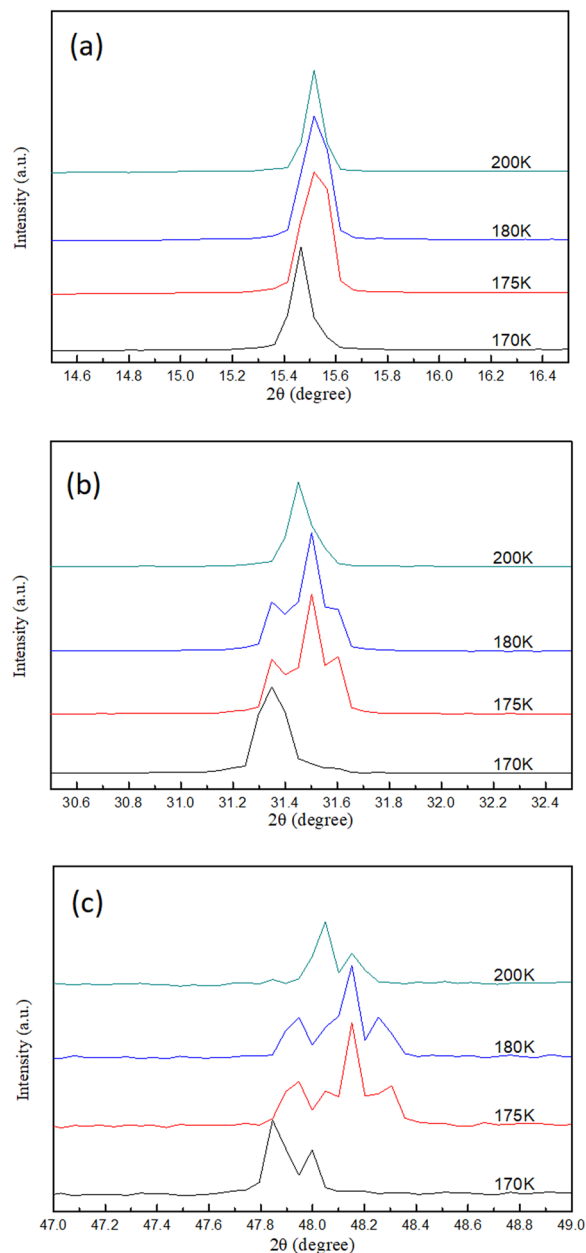
**Figure 7.** Diffraction spectrum of (**a**) (100) (**b**) (200) and (**c**) (300) peak from single crystal XRD measurements of MAPbCl$_3$ at 200–170 K.

**300 K to 200 K.**   Figure 5(a–c) display the single crystal XRD patterns of (100), (200), and (300) crystal planes when the sample was cooled from 300 K to 200 K. As the temperature was decreased, all diffraction patterns moved toward large diffraction angles because of the lattice contraction. No considerable shift in the diffraction angle was observed for all peaks within this temperature range, thereby indicating that the crystal remained in the cubic phase during cooling. The PL spectra shown in Fig. 6(a) remained asymmetric in line shape when the temperature was lowered to 200 K. The peak positions and full width at half maximum (FWHM) were retrieved by fitting of the PL peaks. Figure 6(b,c) show the changes in the PL peak position and line width as a function of temperature. The FWHM became narrower and the emission intensity of peaks 1 and 2 increased when the temperature decreased. The blueshift in peak 2 was slightly enlarged when the temperature was lowered to 200 K. The temperature dependent FWHM of emission peak 1 that correspond to the cubic phase (Fig. 6(c)) is fitted by considering the temperature inhomogeneous broadening ($\Gamma_o$) and the interaction between LO phonons and photoexcited carriers, described by the Fröhlich Hamiltonian[47]. The inset in Fig. 6(c) shows the extracted fitting parameters with values of $\Gamma_o = 44$ meV, LO phonon-photoexcited carrier coupling strength $\gamma_o = 116$ meV, and LO phonon energy $E_{LO} = 32$ meV.
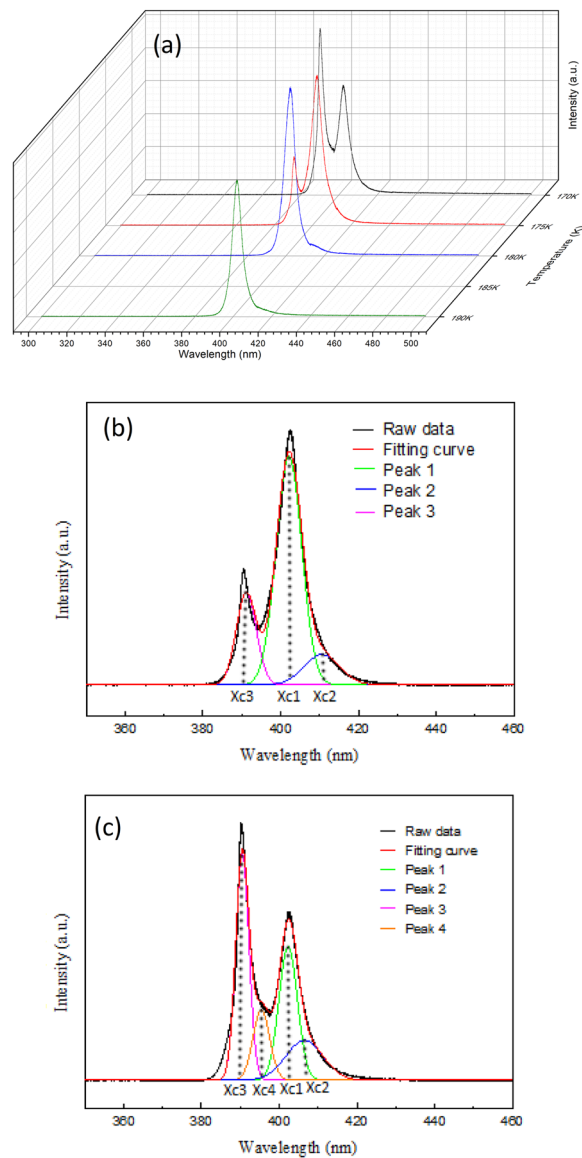
**Figure 8.** (**a**) PL spectra of MAPbCl$_3$ single crystals excited at 266 nm at 190–170 K. (**b**) Fitting of the representative PL spectrum recorded at (**b**) 175 K and (**c**) 170 K in this stage.

**200 K to 170 K.** When the sample was cooled from 200 K to 170 K, two phase transitions occurred in the MAPbCl$_3$ crystal, from cubic to tetragonal (first phase transition) and tetragonal to orthorhombic (second phase transition), as evidenced by the larger shift in diffraction angle and line shape change at 200 K to 180 K and 175 K to 170 K in the XRD spectra shown in Fig. 7(a–c). The first phase transition was majorly induced by the rotational motion around the c-axis of the PbCl$_6^{4+}$ octahedron[48,49]. The second phase transition was activated when the PbCl$_6^{4+}$ octahedron inclined out of the ab plane[50]. An illustration of the 3D MAPbCl$_3$ structure at different crystal phases displayed in Fig. S4 gives a scenario of the structure changes. Figure S5(a) shows the calculated plane spacing (d-spacing) of the (100) planes using the Bragg diffraction law as a function of temperature from 300 K to 180 K (in cubic phase) shown in the XRD data in Fig. 5(a). Therefore, the thermal expansion coefficient of ~2.44 × 10$^{-4}$ K$^{-1}$ of the crystal can be obtained by fitting the slope of the curve in Fig. S5(a). If no phase transition occurs, then the predicted position of the (100) diffraction peak at 170 K should take placed at an angle of 15.55 degree according to the retrieved thermal expansion coefficient. However, the measured (100) peak was at 15.46 degree (see Fig. S5(b)), which is different from the predicted value. Therefore, we infer that phase transitions occurred at this temperature range.

The structure changes were also manifested in the absorption and PL spectra. Figure 8(a) displays the temperature dependent PL spectra recorded from 190 K to 170 K, in which the PL line shape dramatically changed at ~175 K. Different from the previous temperature stage, three emission peaks (Fig. 8(b)) are required to fit the representative PL spectrum recorded at 175 K. Other than the peaks 1 and 2, which were ascribed to the co-existing cubic phase transitions and Cl vacancy[33], a third peak (peak 3) appeared at ~390 nm. This newly emerged peak 3 not only persisted but also continuously grew in intensity when the temperature was further cooled down below 170 K. The presence of the emission peak 3 at temperatures under 175 K was most likely induced by the secondary phase transition, i.e. transition
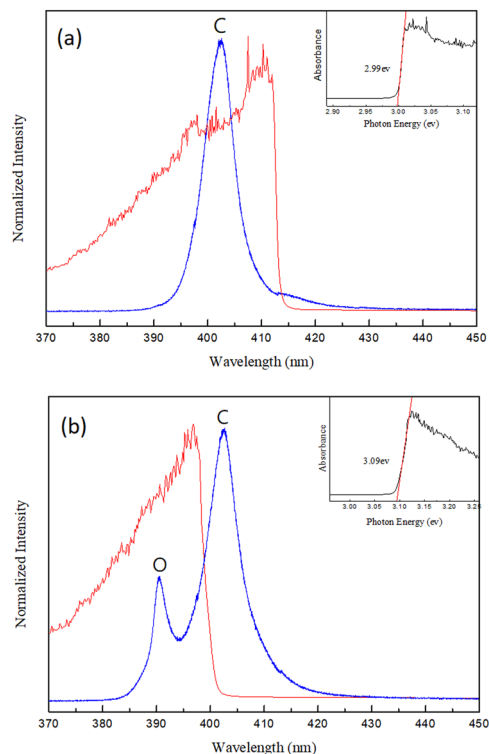
**Figure 9.** Absorption spectra of MAPbCl₃ single crystals excited at 266 nm at (**a**) 180 K and (**b**) 170 K. C and O represent the emission from crystals in cubic and orthorhombic phases, respectively. The insets display the Tauc-plot fitting of absorption edges.

from tetragonal to orthorhombic. The shift in the absorption edge was validated by measuring the temperature dependent absorption spectra. The absorption edge displayed a significant blue shift (from 2.99 eV to 3.09 eV) when the temperature was lowered from 180 K to 175 K as shown in Fig. 9(a,b). We were not able to resolve the first phase transition (from cubic to tetragonal) in the PL/absorption spectra due to the limited temperature resolution (>5 K) and because these two phase transitions were only separated by ~6 K in temperature[51]. Moreover, another new peak 4 appeared at ~395 nm and persisted even at temperature below 170 K when the PL spectrum measured at 170 K was fitted (as shown in Fig. 8(c)). We speculated that this peak was also originated from the Cl vacancy in orthorhombic phase.

**160 K to 20 K.** The temperature dependent single crystal XRD patterns of the crystal planes (100), (200), and (300) obtained from 160 K to 20 K are shown in Fig. 10. No noticeable shift in diffraction angle and change in line shape can be observed, thereby implying that the crystal remained relatively stable in orthorhombic phase throughout this temperature stage. The PL spectra obtained from 130 K to 20 K are displayed in Fig. 11(a,b). At the initial cooling stage, most PL peak positions remained nearly unchanged except peak 2, which moved toward lower energy as the temperature dropped (as shown in Fig. 11(c)). In addition to the increasing in emission intensity, the PL line shape also dramatically changed between 390 and 410 nm when the temperature dropped below 90 K. Several sharp spectral lines gradually emerged during cooling, as shown in Fig. 11(b,c). The representative PL spectrum with labelled sharp spectral lines (peak a to peak i) between 390 and 450 nm at 20 K is displayed in Fig. 12. The offset energy of the sharp lines relative to the band edge of the orthorhombic phase (peak 3) at 20 K was measured and is summarized in Table 2. The measured offset energy had the same order as the vibrational/librational modes of the cation and metallic frame. Therefore, we carefully crosschecked and compared these values with the results reported in ref. [42], in which Raman bands of the polycrystalline MAPbCl₃ samples were recorded in orthorhombic phase and the associated translational and librational motions of different groups were assigned. We uncovered that the energies of these sharp spectral lines corresponded to either a single or a combination of the translational and/or librational motions of MA⁺. This finding has never been reported in other lead halide perovskites, such as MAPbI₃ or MAPbBr₃. We speculate that the MAPbCl₃ single crystal has stronger polar nature and dipole momentum because of the enhanced polarization between $PbCl_6^-$ and MA⁺ due to the higher electron negativity of the chloride atoms. This result is relatively similar to those for inorganic polar semiconductors (such as GaAs). Therefore, vibronic coupling occurred between the photoexcited carriers and the translational and librational motions from the MA groups, and this phenomenon was more enhanced in MAPbCl₃. With decreasing temperature, the intensity and FWHM of those vibronic replicas became strong and narrow due to the long translational/librational mode dephasing time. It will be interesting to further investigate the dynamics of these vibronic replicas.

In the end, we studied the electronic characteristics of the MAPbCl₃ single crystal using I–V and Hall measurements. The schematics of the devices are displayed in the inset of Figs S6 and S7. The as-grown MAPbCl₃ single crystal was determined as an n-type semiconductor with a carrier concentration of ~$2.63 \times 10^{11}$ cm⁻³ and a
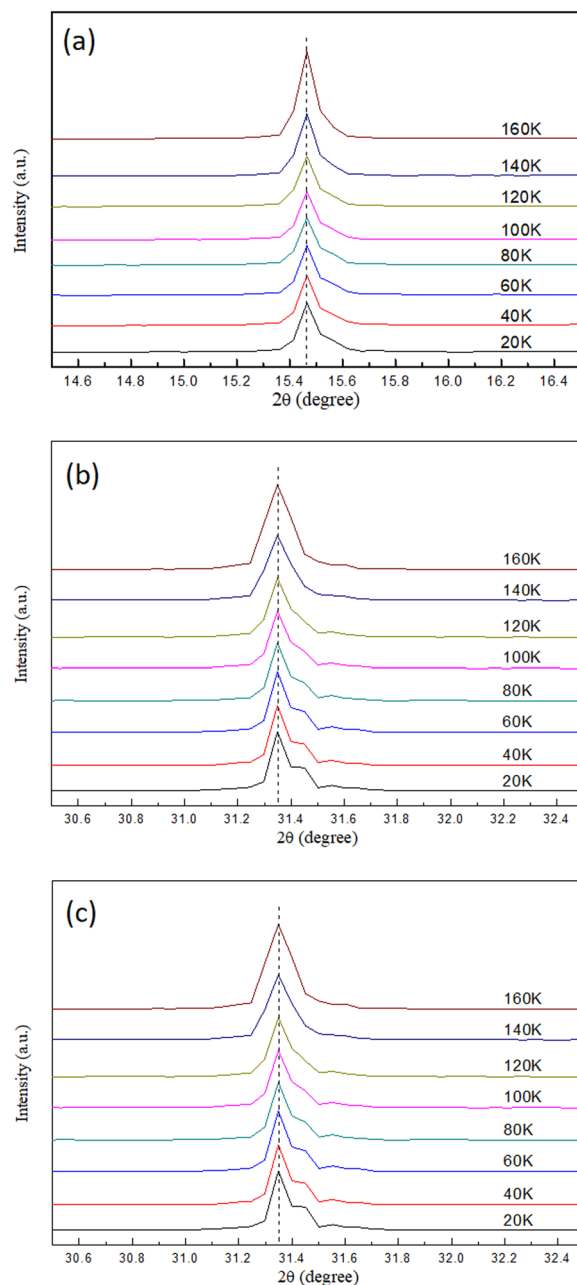
**Figure 10.** Diffraction spectrum of (**a**) (100) (**b**) (200) and (**c**) (300) peak from single crystal XRD measurements of MAPbCl$_3$ at 160–20 K.

mobility of ~4.14 cm$^2$/V•s according to the Hall measurements as shown in Fig. S6. The lower carrier mobility of MAPbCl$_3$ compared with that of MAPbI$_3$ and MAPbBr$_3$[52] is due to the stronger ionic nature of the Pb-Cl bonding. Figure S7(a,b) display the I–V curves of the crystal under dark and illumination. The I–V responses showed linear behavior with scanned bias from 0–40 V. A conductivity of ~$1.8 \times 10^{-8} \Omega^{-1} cm^{-1}$ was estimated and was in good agreement with earlier reports[36]. When illuminated with a 405 nm laser, the conductivity of the crystal increased by approximately an order of magnitude to ~$9.7 \times 10^{-8} \Omega^{-1} cm^{-1}$ as shown in Fig. S7(b).

## Conclusions

The crystal structures, photophysical and electronic characteristics of MAPbCl$_3$ single crystals were studied using temperature dependent XRD, optical spectroscopy techniques, I–V, and Hall measurements. The crystal went through two phase changes, namely, cubic to tetragonal (at ~180 K) and tetragonal to orthorhombic (at ~175 K) when the temperature decreased from 300 K to 20 K. The crystal surface was sensitive to the environment, thereby implying that MAPbCl$_3$ perovskites can be utilized as gas sensors. In contrast to our earlier studies on MAPbBr$_3$ single crystals[33], vibronic replicas were observed for the first time at temperatures under 90 K because of the higher electron negativity of chloride atom that led to the stronger polar nature of the crystal. This result suggests
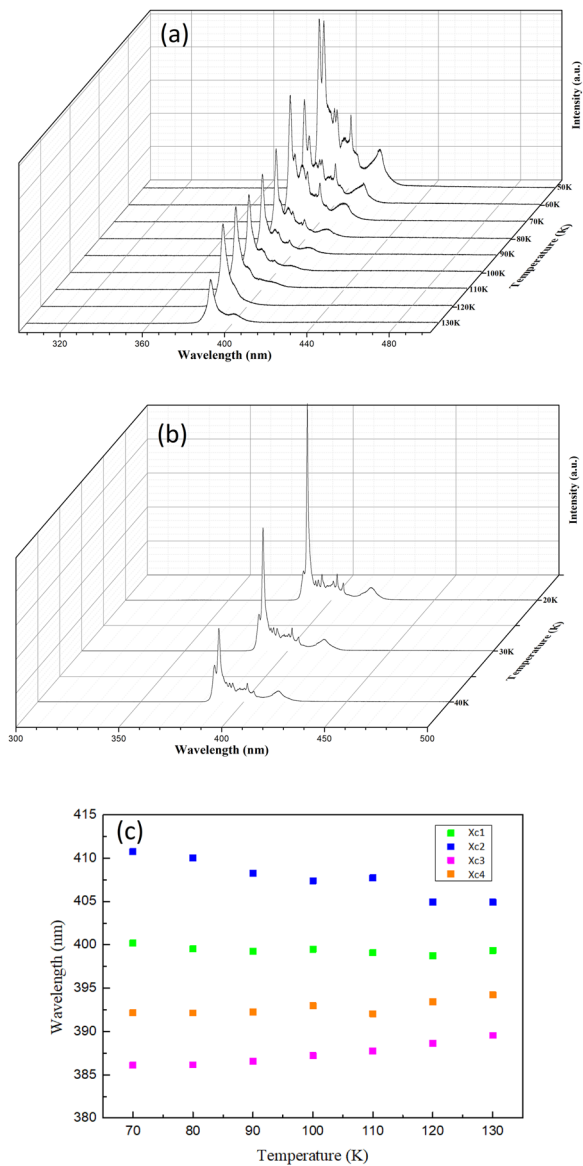
**Figure 11.** PL spectra of MAPbCl$_3$ single crystals excited at 266 nm at (**a**) 130–50 K (**b**) 40–20 K. (**c**) Peak position as a function of temperature from 130 K to 70 K of peaks 1 to 4 from the fitting in Fig. 8(c).
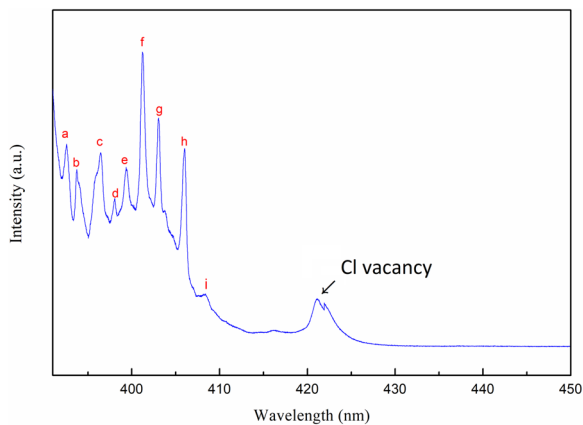


**Figure 12.** Representative PL spectrum between 390 nm and 450 nm at 20 K with excitation at 266 nm. The sharp spectral lines are labelled from a to i. The peak at ~422 nm is due to the Cl vacancy.

| Peak label | Energy offset $\Delta E$ (meV) | Peak assignment (ref. [42]) |
|---|---|---|
| a | 29.5 | T'/R' of MA$^+$ (238 cm$^{-1}$ ~29.5 meV) |
| b | 38.84 | T'/R' of MA$^+$ (321 cm$^{-1}$ ~39.8 meV) |
| c | 60.49 | MA$^+$ torsion (483 cm$^{-1}$ ~60 meV) |
| d | 76.39 | T'/R'of MA$^+$(321 cm$^{-1}$ ~39.8 meV) + T'/R'of MA$^+$(321 cm$^{-1}$ ~39.8 meV) |
| e | 86.54 | T'/R' of MA$^+$(238 cm$^{-1}$ ~29.5 meV) + MA$^+$ torsion (483 cm$^{-1}$ ~60 meV) |
| f | 100.32 | T'/R' of MA$^+$ (321 cm$^{-1}$ ~39.8 meV) + MA$^+$ torsion (483 cm$^{-1}$ ~60 meV) |
| g | 115.10 | MA$^+$ rocking (923 cm$^{-1}$ ~114 meV) |
| h | 137.39 | C-N stretch (977 cm$^{-1}$ ~121 meV) + T'/R' of MA$^+$ (119 cm$^{-1}$ ~14.7 meV) |
| i | 155.33 | C-N stretch (1263 cm$^{-1}$ ~156 meV) |

**Table 2.** The measured offset energy of sharp spectral lines at 20 K shown in Fig. 12 and their assignments to the translational/librational modes of MA$^+$.

that, unlike the other organo-lead halide-based perovskites, the photoexcited carriers are able to interact with the organic cations and transfer their energy into vibrational/librational motions of organic molecules. The pristine crystal was demonstrated as an n-type semiconductor at 300 K with a carrier concentration of ~$2.63 \times 10^{11}$ cm$^{-3}$, a mobility of 4.14 cm$^2$/V•s, and a conductivity of $1.8 \times 10^{-8}$ $\Omega^{-1}cm^{-1}$ under dark conditions. The conductivity increased by approximately an order of magnitude when it was illuminated with a 405 nm laser. Our new findings can help future development of using MAPbCl$_3$ perovskites for UV optoelectronics.

## References

1. Etgar, L. *et al.* Mesoscopic CH$_3$NH$_3$PbI$_3$/TiO$_2$ Heterojunction Solar Cells. *J. Am. Chem. Soc.* **134**, 17396–17399 (2012).
2. Jeon, N. J. *et al.* Compositional engineering of perovskite materials for high-performance solar cells. *Nature* **517**, 476–480 (2015).
3. Zhou, H. *et al.* Interface engineering of highly efficient perovskite solar cells. *Science* **345**, 542–546 (2014).
4. Lee, M. M., Teuscher, J., Miyasaka, T., Murakami, T. N. & Snaith, H. J. Efficient Hybrid Solar Cells Based on Meso-Superstructured Organometal Halide Perovskites. *Science* **338**, 643–647 (2012).
5. Liu, M., Johnston, M. B. & Snaith, H. J. Efficient planar heterojunction perovskite solar cells by vapour deposition. *Nature* **501**, 395–398 (2013).
6. Tan, Z.-K. *et al.* Bright light-emitting diodes based on organometal halide perovskite. *Nat Nano* **9**, 687–692 (2014).
7. Xing, G. *et al.* Low-temperature solution-processed wavelength-tunable perovskites for lasing. *Nat Mater* **13**, 476–480 (2014).
8. Deschler, F. *et al.* High Photoluminescence Efficiency and Optically Pumped Lasing in Solution-Processed Mixed Halide Perovskite Semiconductors. *The Journal of Physical Chemistry Letters* **5**, 1421–1426 (2014).
9. Fang, Y., Dong, Q., Shao, Y., Yuan, Y. & Huang, J. Highly narrowband perovskite single-crystal photodetectors enabled by surface-charge recombination. *Nat Photon* **9**, 679–686 (2015).
10. Dou, L. *et al.* Solution-processed hybrid perovskite photodetectors with high detectivity. *Nat. Commun.* **5**, 5404 (2014).
11. Niu, G., Guo, X. & Wang, L. Review of recent progress in chemical stability of perovskite solar cells. *Journal of Materials Chemistry A* **3**, 8970–8980 (2015).
12. Misra, R. K. *et al.* Temperature- and Component-Dependent Degradation of Perovskite Photovoltaic Materials under Concentrated Sunlight. *The Journal of Physical Chemistry Letters* **6**, 326–330 (2015).
13. Snaith, H. J. *et al.* Anomalous Hysteresis in Perovskite Solar Cells. *The Journal of Physical Chemistry Letters* **5**, 1511–1515 (2014).
14. Raga, S. R. *et al.* Influence of Air Annealing on High Efficiency Planar Structure Perovskite Solar Cells. *Chemistry of Materials* **27**, 1597–1603 (2015).
15. Han, Y. *et al.* Degradation observations of encapsulated planar CH$_3$NH$_3$PbI$_3$ perovskite solar cells at high temperatures and humidity. *Journal of Materials Chemistry A* **3**, 8139–8147 (2015).
16. Wehrenfennig, C., Liu, M., Snaith, H. J., Johnston, M. B. & Herz, L. M. Charge carrier recombination channels in the low-temperature phase of organic-inorganic lead halide perovskite thin films. *APL Materials* **2**, 081513 (2014).
17. Wu, K. *et al.* Temperature dependent excitonic photoluminescence of hybrid organometal halide perovskite films. *Physical Chemistry Chemical Physics* **16**, 22476–22481 (2014).
18. Yang, Y. *et al.* Comparison of Recombination Dynamics in CH$_3$NH$_3$PbBr$_3$ and CH$_3$NH$_3$PbI$_3$ Perovskite Films: Influence of Exciton Binding Energy. *The Journal of Physical Chemistry Letters* **6**, 4688–4692 (2015).
19. Yan, J., Ke, X., Chen, Y., Zhang, A. & Zhang, B. Effect of modulating the molar ratio of organic to inorganic content on morphology, optical absorption and photoluminescence of perovskite CH$_3$NH$_3$PbBr$_3$ films. *Applied Surface Science* **351**, 1191–1196 (2015).
20. Sheng, R. *et al.* Methylammonium Lead Bromide Perovskite-Based Solar Cells by Vapor-Assisted Deposition. *The Journal of Physical Chemistry C* **119**, 3545–3549 (2015).
21. Wen, X. *et al.* Mobile Charge-Induced Fluorescence Intermittency in Methylammonium Lead Bromide Perovskite. *Nano Letters* **15**, 4644–4649 (2015).
22. Christians, J. A., Manser, J. S. & Kamat, P. V. Multifaceted Excited State of CH$_3$NH$_3$PbI$_3$. Charge Separation, Recombination, and Trapping. *The Journal of Physical Chemistry Letters* **6**, 2086–2095 (2015).
23. Shi, D. *et al.* Low trap-state density and long carrier diffusion in organolead trihalide perovskite single crystals. *Science* **347**, 519–522 (2015).
24. Saidaminov, M. I. *et al.* High-quality bulk hybrid perovskite single crystals within minutes by inverse temperature crystallization. *Nat. Commun.* **6**, 7586 (2015).
25. Mante, P.-A., Stoumpos, C. C., Kanatzidis, M. G. & Yartsev, A. Electron–acoustic phonon coupling in single crystal CH$_3$NH$_3$PbI$_3$ perovskites revealed by coherent acoustic phonons. *Nat. Commun.* **8**, 14398 (2017).
26. Park, J.-S. *et al.* Electronic Structure and Optical Properties of α-CH$_3$NH$_3$PbBr$_3$ Perovskite Single Crystal. *The Journal of Physical Chemistry Letters* **6**, 4304–4308 (2015).

27. Dong, Q. *et al.* Electron-hole diffusion lengths > 175 μm in solution-grown CH3NH3PbI3 single crystals. *Science* **347**, 967–970 (2015).
28. Yang, Y. *et al.* Low surface recombination velocity in solution-grown CH₃NH₃PbBr₃ perovskite single crystal. *Nat. Commun.* **6**, 7961 (2015).
29. Yamada, T. *et al.* Fast Free-Carrier Diffusion in CH₃NH₃PbBr₃ Single Crystals Revealed by Time-Resolved One- and Two-Photon Excitation Photoluminescence Spectroscopy. *Advanced Electronic Materials* **2**, 1500290 (2016).
30. Wu, B. *et al.* Discerning the Surface and Bulk Recombination Kinetics of Organic–Inorganic Halide Perovskite Single Crystals. *Advanced Energy Materials* **6**, 1600551 (2016).
31. Tilchin, J. *et al.* Hydrogen-like Wannier–Mott Excitons in Single Crystal of Methylammonium Lead Bromide Perovskite. *ACS Nano* **10**, 6363–6371 (2016).
32. Murali *et al.* Surface Restructurinig of Hybrid Perovskite Crystals. *ACS Energy Lett.* **1**, 1119–1126 (2016).
33. Wang, K. H., Li, L. C., Shellaiah, M. & Sun, K. W. Structural and Photophysical Properties of Methylammonium Lead Tribromide (MAPbBr₃) Single Crystals. *Sci. Reports* **7**, 13643 (2017).
34. Miyata, K. *et al.* Large Polarons in Lead Halide Perovskites. *Sci. Adv.* **3**, e1701217 (2017).
35. Adinolfi, V. *et al.* Fast and Sensitive Solution-Processed Visible-Blind Perovskite UV Photodetectors. *Adv. Mater.* **28**, 7264–7268 (2016).
36. Maculan, G. *et al.* CH₃NH₃PbCl₃ Single Crystal: Inverse Temperature Crystallization and Visible-Blind UV-Photodetector. *J. Phys. Chem. Lett.* **6**, 3781–3786 (2015).
37. Cheng, X. *et al.* Crystal Orientation-dependent Optoelectronic Properties of MAPbCl₃ Single. *Crystals. J. Mater. Chem. C* **6**, 1579–1586 (2018).
38. Wu, X. *et al.* Trap States in Lead Iodide Perovskites. *Journal of the American Chemical Society* **137**, 2089–2096 (2015).
39. Zhang, F. *et al.* Comparative studies of optoelectrical properties of prominent PV materials: Halide Perovskite, CdTe, and GaAs. *arXiv 1907.03434* (2019).
40. Eperon, G. E. *et al.* The Importance of Moisture in Hybrid Lead Halide Perovskite Thin Film Fabrication. *ACS Nano* **9**, 9380–9393 (2015).
41. Pathak, S. *et al.* Atmospheric Influence upon Crystallization and Electronic Disorder and Its Impact on the Photophysical Properties of Organic–Inorganic Perovskite Solar Cells. *ACS Nano* **9**, 2311–2320 (2015).
42. Maalej, A. *et al.* Phase Transitions and Crystal Dynamics in the Cubic Perovskite CH₃NH₃PbCl₃. *Solid State Communications* **103**, 279–284 (1997).
43. Chen, Q. *et al.* Multiple-Stage Structure Transformation of Organic-Inorganic Hybrid Perovskite CH₃NH₃PbI₃. *Phys. Rev. X* **6**, 031042 (2016).
44. Glaser, T. *et al.* Infrared Spectroscopic Study of Vibrational Modes in Methylammonium Lead Halide Perovskites. *The Journal of Physical Chemistry Letters* **6**, 2913–2918 (2015).
45. Xie, L.-Q. *et al.* Organic-inorganic interactions of single crystalline organolead halide perovskites studied by Raman spectroscopy. *Physical Chemistry Chemical Physics* **18**, 18112–18118 (2016).
46. Niemann, R. G. *et al.* Halogen Effects on Ordering and Bonding of CH3NH3+ in CH3NH3PbX3 (X = Cl, Br, I Hybrid Perovskites: A Vibrational Spectroscopic Study. *J. Phys. Chem. C* **120**, 2509–2519 (2016).
47. Dar, M. I. *et al.* Origin of unusual bandgap shift and dual emission in organic-inorganic lead halide perovskites. *Sci. Adv.* **2**, e1601156 (2016).
48. Kawamura, Y., Mashiyama, H. & Hasebe, K. Structural Study on Cubic–Tetragonal Transition of CH₃NH₃PbI₃. *Journal of the Physical Society of Japan* **71**, 1694–1697 (2002).
49. Wehrenfennig, C., Liu, M., Snaith, H. J., Johnston, M. B. & Herz, L. M. Charge carrier recombination channels in the low-temperature phase of organic-inorganic lead halide perovskite thin films. *APL Materials* **2**, 081513 (2014).
50. Poglitsch, A. & Weber, D. Dynamic disorder in methylammoniumtrihalogenoplumbates (II observed by millimeter-wave spectroscopy. *The Journal of Chemical Physics* **87**, 6373–6378 (1987).
51. Onoda-Yamamuro, N., Matsuo, T. & Suga, H. Calorimetric and IR Spectroscopic Studies of Phase Transitions in Methylammonium Trihalogenoplumblates (II). *J. Phys. Chem. Solids* **51**, 1383–1395 (1990).
52. Herz, L. M. Charge-Carrier Mobilities in Metal Halide Perovskites: Fundamental Mechanisms and Limits. *ACS Energy Lett* **2**, 1539–1548 (2017).

## Acknowledgements

## Author Contributions

H.P.H., L.C.L., M.S. and K.W.S. designed the experiments. H.P.H. prepared the single crystals and carried out the XRD, Raman, PL and absorption measurements. L.C.L. conducted the Hall and I-V experiments. M.S. implemented microscopy experiments. K.W.S. wrote the manuscript and all authors have given approval to the final version of the manuscript.

## Additional Information

**Supplementary information** accompanies this paper at https://doi.org/10.1038/s41598-019-49926-z.

**Competing Interests:** The authors declare no competing interests.

**Publisher's note** Springer Nature remains neutral with regard to jurisdictional claims in published maps and institutional affiliations.